Tectonics®

RESEARCH ARTICLE
10.1029/2021TC006808

Key Points:

- We quantify via numerical modeling the influence of denudation on postrift faulting along divergent margins
- Crust–mantle coupling, denudation, and preexistence of weakness zones control reactivation of faults in margins during the postrift phase
- Flexural stresses created by erosional unloading of the margin in a decoupled lithosphere induce faulting in the continental interior

Supporting Information:

Supporting Information may be found in the online version of this article.

Correspondence to:

R. M. Silva and V. Sacek,
rafael.m.silva@alumni.usp.br;
sacek@usp.br

Citation:

Silva, R. M., & Sacek, V. (2022). Influence of surface processes on postrift faulting during divergent margins evolution. *Tectonics*, *41*, e2021TC006808. https://doi.org/10.1029/2021TC006808

Received 12 MAR 2021
Accepted 31 DEC 2021

Influence of Surface Processes on Postrift Faulting During Divergent Margins Evolution

R. M. Silva[1] and V. Sacek[1]

[1]Departamento de Geofísica, Instituto de Astronomia, Geofísica e Ciências Atmosféricas, Universidade de São Paulo, São Paulo, Brazil

Abstract We used thermomechanical numerical models to simulate the formation and evolution of divergent continental margins since continental rifting, taking into account surface processes of erosion of the continental escarpment. We found that the degree of crust–mantle coupling, the magnitude and extent of erosion of the coastal landscape, and the preexistence of weakness zones in the continental crust are important elements that control the reactivation of faults along divergent margins during the postrift phase. The numerical experiments indicated that the presence of a lower crust with a relatively low viscosity, facilitating the decoupling of the upper crust and the development of hyperextended margins, could also contribute to the development and/or reactivation of normal faults in the interior of the continent when the margin is continually subjected to differential denudation and consequent flexural response of the lithosphere. This effect is suppressed in scenarios where the lower crust presents a relatively high viscosity, consequently inducing the coupling of the upper crust with the lithospheric mantle. In this case, the long wavelength of the flexural response of a coupled lithosphere to erosional unloading has a minor impact on the reactivation of faults in the upper crust. As an application of our model, we propose that the combination of a decoupled continental lithosphere, escarpment retreat due to erosion, and the preexistence of shear zones parallel to the coast contributed to the development of postrift Cenozoic tectonism in southeastern Brazil.

1. Introduction

From the computational point of view, in recent decades, two independent branches of numerical codes were developed to study the formation and evolution of divergent continental margins:

1. One branch is defined as landscape evolution models (LEMs), dedicated to simulate how the landscape evolves as a combination of the interaction between surface processes of erosion and sedimentation along with isostasy and flexure of the lithosphere, mainly focused on the postrift phase of divergent margins (e.g., Braun, 2018; A. Gilchrist & Summerfield, 1990; A. R. Gilchrist et al., 1994; Kooi & Beaumont, 1994; Sacek et al., 2012; van der Beek et al., 2002).
2. The second branch represents thermomechanical models constructed to simulate the lithospheric thinning since the onset of rifting (e.g., Braun & Beaumont, 1989; Brune et al., 2014; Huismans & Beaumont, 2003; Lavier & Manatschal, 2006).

In parallel, and especially in the last years, new numerical codes were developed to integrate LEMs in thermomechanical models, evaluating how the coupling and possible feedback mechanisms exist between surface and tectonic processes in divergent margins. Burov and Cloetingh (1997) presented an example of the interaction of surface and thermomechanical processes during and after the rifting phase. The authors showed the feedback between erosion and sedimentation of the surface, ductile flow of lower crust, and the flexural response of the lithosphere. Following this work, other models showed the importance of surface processes affecting the thermal and, hence, rheological structure of the lithosphere (Andrés-Martínez et al., 2019; Beucher & Huismans, 2020; Pérez-Gussinyé et al., 2020), even influencing the magmatic activity (Sternai, 2020). Recently, Theunissen and Huismans (2019) identified feedbacks between erosion and deposition and tectonic processes on structural style of rift and divergent margin formation due to the efficiency of surface processes.

However, with few exceptions (e.g., Burov & Cloetingh, 1997), these coupled thermomechanical models focused mainly on the rifting stage of the margin development, and little attention was given to the impact of surface

10.1029/2021TC006808

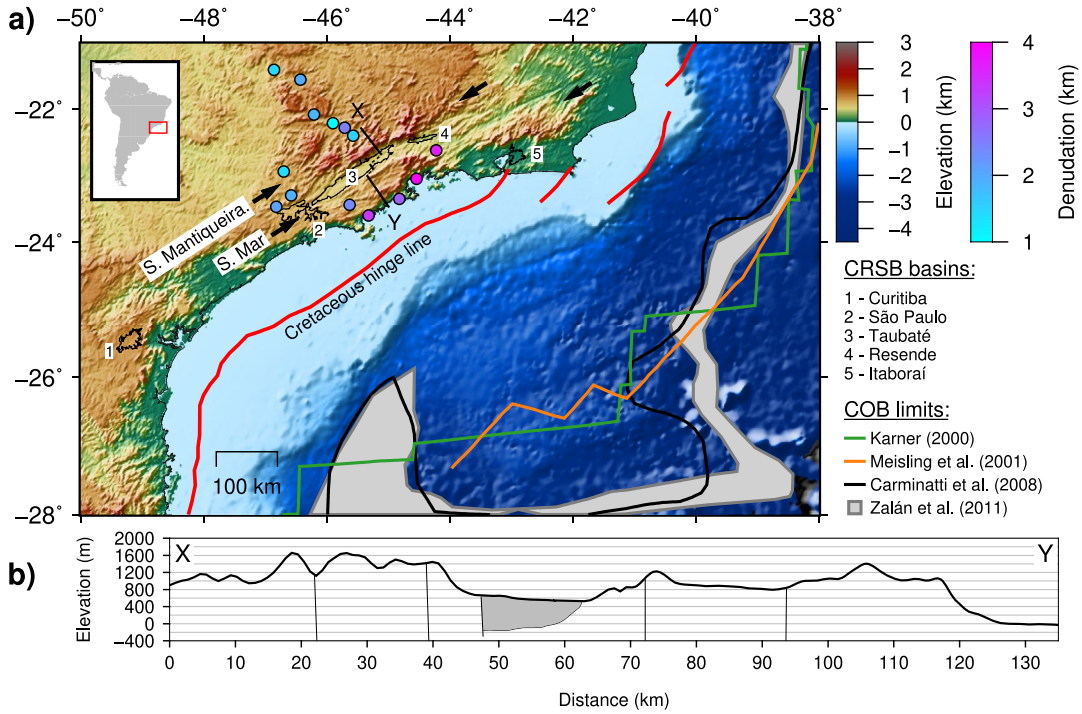

Figure 1. (a) Topographic/bathymetric map of southeastern Brazil. The arrows indicate the two parallel escarpments in southeastern Brazil: the Serra do Mar and Serra da Mantiqueira escarpments. These two escarpments are separated by an elongated depression associated with the Continental Rift of Southeastern Brazil (CRSB). The main basins of the CRSB are indicated by numbers: 1, Curitiba; 2, São Paulo; 3, Taubaté; 4, Resende; 5, Itaboraí. The thick red line indicates the Cretaceous hinge line extracted from Karner and Gambôa (2007). The other lines indicate the continent–ocean boundary (COB) presented by different authors (Carminatti et al., 2008; Karner, 2000; Meisling et al., 2001; Zalán et al., 2011). COB compilation extracted from Rigoti (2015). The circles indicate the postrift denudation based on thermochronological data (Cogné et al., 2011) assuming a geothermal gradient of 30°C. (b) Topographic profile crossing the Serra da Mantiqueira and Serra do Mar escarpments indicated by *X*–*Y* in the map. The gray region indicates the Cenozoic sedimentation preserved between the two escarpments. Profile extracted from Cogné et al. (2012).

processes on the onshore tectonic evolution of the continental lithosphere during the postrift evolution of divergent margins, tens of millions of years after the end of lithospheric stretching.

In the present work, we evaluated how surface processes can affect the stress field in the continental lithosphere of divergent margins, taking into account the erosive retreat of the coastal escarpment in a visco-plastic thermomechanical model, simulating the evolution of divergent margins since the onset of lithospheric stretching. We observed that the strain rate pattern induced in the continental margin during the postrift phase depends on the magnitude of the erosion of the coastal escarpment and the degree of coupling between crust and lithospheric mantle. We suggest that the reactivation of normal faults in the continental interior induced by the flexural response of the plate to escarpment denudation is promoted when the lithosphere is decoupled, compatible to a low effective elastic thickness. On the other hand, in the scenarios with coupled lithosphere, postrift reactivation presents smaller magnitude, occurring essentially in the coastal plain and in the offshore domain.

As a geological example, we present the case of southeastern Brazil (Figure 1a) where a postrift tectonism induced the formation of marging-parallel basins in the continent, preserving a sedimentary package of up to 800 m (Figure 1b) with ages ranging from Paleogene to Quaternary (Riccomini, 1989). This tectonic event produced a series of elongated basins (Figure 1a) distributed for nearly 900 km along the margin, denominated as Continental Rift of Southeastern Brazil (CRSB; Riccomini et al., 2004), following the NE-trend of Precambrian rocks of the Ribeira Belt. The origin of the CRSB cannot be directly related to the Early Cretaceous opening of the South Atlantic, which occurred more than 60 Myr before the development of these interior basins. We propose that the combination of differential denudation of the coastal escarpments with a decoupled continental lithosphere

created tensional stresses in the upper crust necessary for the development of the CRSB in the continental interior over the Ribeira Belt.

2. Methods

2.1. Model Description

To simulate the formation and evolution of continental margins during and after lithospheric stretching, we used the finite element code MANDYOC (Sacek, 2017) to solve the equations for conservation of mass, momentum, and energy for incompressible viscous flow with infinite Prandtl number:

$$u_{i,i} = 0 \tag{1}$$

$$\sigma_{ij,j} - g\rho\delta_{i2} = 0 \tag{2}$$

$$\frac{\partial T}{\partial t} + u_i T_{,i} = \kappa T_{,ii} + H/c_p - \alpha T g u_2/c_p \tag{3}$$

in which

$$\sigma_{ij} = -P\delta_{ij} + \eta(u_{i,j} + u_{j,i}) \tag{4}$$

$$\rho = \rho_0 (1 - \alpha(T - T_0)) \tag{5}$$

with

$$i, j = 1, 2$$

where t is time, u_i is the ith velocity component, g is gravity acceleration, ρ is the effective density, α is the volumetric expansion coefficient, T is temperature, ρ_0 is the reference density at $T = T_0 = 0°C$, κ is the thermal diffusivity, H is the heat production per unit mass, P is the total pressure, c_p is the specific heat, σ is the stress tensor, η is the rock effective viscosity, and δ_{ij} is the Kronecker delta. In this notation, repeated indices indicate an addition and $T_{,i}$ is the partial derivative of T relative to the coordinate x_i. The last two terms in Equation 3 are the internal heating production and the adiabatic heating, respectively.

We adopted a visco-plastic rheology where the effective viscosity η combines nonlinear power law viscous rheology and a plastic yield criterion. The viscous component is given by

$$\eta_{visc} = C \cdot A^{-1/n} \cdot \dot{\varepsilon}_{II}^{\frac{1-n}{n}} \cdot \exp\left(\frac{Q + V \cdot P}{nRT}\right) \tag{6}$$

in which C is a scale factor, A is the preexponential factor, n is the power law exponent, $\dot{\varepsilon}_{II}$ is the square root of the second invariant of the deviatoric strain rate tensor $\left(\dot{\varepsilon}'_{ij}\dot{\varepsilon}'_{ij}/2\right)^{1/2}$, Q is the activation energy, V is the activation volume, and R is the gas constant. The values of A, n, Q, and V for crust and mantle rocks were extracted from Karato and Wu (1993) and Gleason and Tullis (1995). The adopted values of each constant parameter indicated in the conservation equations are shown in Tables 1 and 2.

In the plastic regime, brittle failure is achieved when the stress surpasses the limit given by the Drucker–Prager criterion:

$$\sigma_{yield} = c_0 \cdot \cos\phi + P \cdot \sin\phi \tag{7}$$

where ϕ and c_0 are the internal angle of friction and the internal cohesion of the rock, respectively. To facilitate the formation of localized deformation during lithospheric stretching, we adopted strain-softening effects, where the values of ϕ and c_0 vary as a function of cumulative strain ε (Huismans & Beaumont, 2003). We used the procedure adopted by Salazar-Mora et al. (2018), where c_0 and ϕ linearly decrease from 20 to 4 MPa and from 15° to 2°, respectively, for accumulated strain values between 0.05 and 1.05. Below and above these limits, c_0 and ϕ are assumed constant. This total accumulated strain and the different materials are tracked by particles that permeate the numerical domain (Gerya, 2019), initially assuming 40 particles per element.

Table 1
Physical Parameters for the Different Layers of the Numerical Scenarios

Description	Symbol	Unit	Air	Upper crust	Lower crust	Lithospheric mantle	Asthenosphere
Reference density	ρ_0	kg/m^3	1	2,700	2,800	3,354	3,378
Creep flow law	–	–	–	Quartz	Quartz	Dry olivine	Wet olivine
Preexponent constant	A	Pa^{-n}/s	1.0×10^{-18}	8.574×10^{-28}	8.574×10^{-28}	2.4168×10^{-15}	1.393×10^{-14}
Activation energy	Q	kJ/mol	0	222	222	540	429
Power law exponent	n	–	1	4	4	3.5	3
Activation volume	V	m^3/mol	0	0	0	25×10^{-6}	15×10^{-6}
Scale factor	C	–	1	1	1, 40	1	1
Heat production	H	W/kg	0	9.26×10^{-10}	2.86×10^{-10}	9.0×10^{-12}	0

Note. Parameters extracted from Karato and Wu (1993) for olivine and Gleason and Tullis (1995) for quartz.

The effective nonlinear viscosity is given by the combination of the plastic and the viscous components (Moresi & Solomatov, 1998):

$$\eta = \min\left(\eta_{plast}, \eta_{visc}\right) = \min\left(\frac{\sigma_{yield}}{2\dot{\varepsilon}_{II}}, \eta_{visc}\right) \tag{8}$$

Additionally, the viscosity was limited by the minimum and maximum values of 10^{18} and 10^{25} Pa s, respectively.

2.2. Model Setup

The numerical domain comprises $1{,}600 \times 300$ km^2 (Figure 2a), composed of a regular mesh with square elements of 1×1 km^2, resulting in 480,000 elements. We adopted Q1P0 finite elements, which are bilinear in velocity and constant in pressure. The domain is subdivided into asthenosphere, lithospheric mantle, lower crust, upper crust, and air, with each different composition tracked by particles that permeate the finite elements, as described in the previous section. Crustal thickness is based on Assumpção et al. (2013) and lithosphere thickness is estimated from Artemieva (2006). To simulate the free surface, we adopted the "sticky air" approach (e.g., Crameri et al., 2012), taking into account a 40-km-thick layer with a relatively low-viscosity material but with a compatible density with the atmospheric air (see Table 1).

The boundary conditions for the velocity field simulate the lithospheric stretching assuming a reference frame fixed on the lithospheric plate on the left side of the model, and the plate on the right side moves rightward with a velocity $v_{\text{rift}} = 1$ cm/year (Figure 2a). This velocity is compatible with the extension velocity between South America and Southern Africa at the latitude of the Santos Basin during the rifting phase (Brune et al., 2014). The velocity field at the left and right boundaries of the model is chosen to ensure conservation of mass and is symmetrical, assuming the adopted reference frame moves to the right with a velocity $v_{\text{rift}}/2$ relative to the left plate (Appendix A). The inflow on the vertical boundaries below the lithosphere compensates for outflow. Additionally, free slip was applied on the top and bottom of the numerical domain. The adopted boundary conditions for velocity are adopted in order to analyze the influence of the surface processes on the tectonic evolution of the continental margin formed on the left part of the model.

Table 2
Fixed Parameters for the Numerical Scenarios

Description	Symbol	Value	Unit
Volumetric expansion coefficient	α	3.28×10^{-5}	K^{-1}
Thermal diffusivity	κ	10^{-6}	m^2/s
Specific heat capacity	c_p	1,250	J/kg/K
Half width for the denudation function	x_σ	200	km
Position of maximum denudation	x_c	800	km
Maximum denudation rate	k_{sp}	8×10^{-4}	m/year
Sea level relative to the initial altitude	h_{sl}	−1,500	m

The initial temperature structure is depth dependent and is 0°C at the surface and 1300°C at the base of the lithosphere at 130 km. With these boundary conditions, the initial temperature structure in the interior of the lithosphere is given by the solution of the following equation:

$$\kappa \frac{\partial^2 T(z)}{\partial z^2} + \frac{H(z)}{c_p} = 0 \tag{9}$$

where $H(z)$ is the internal heat production of the different layers, as indicated in Table 1.

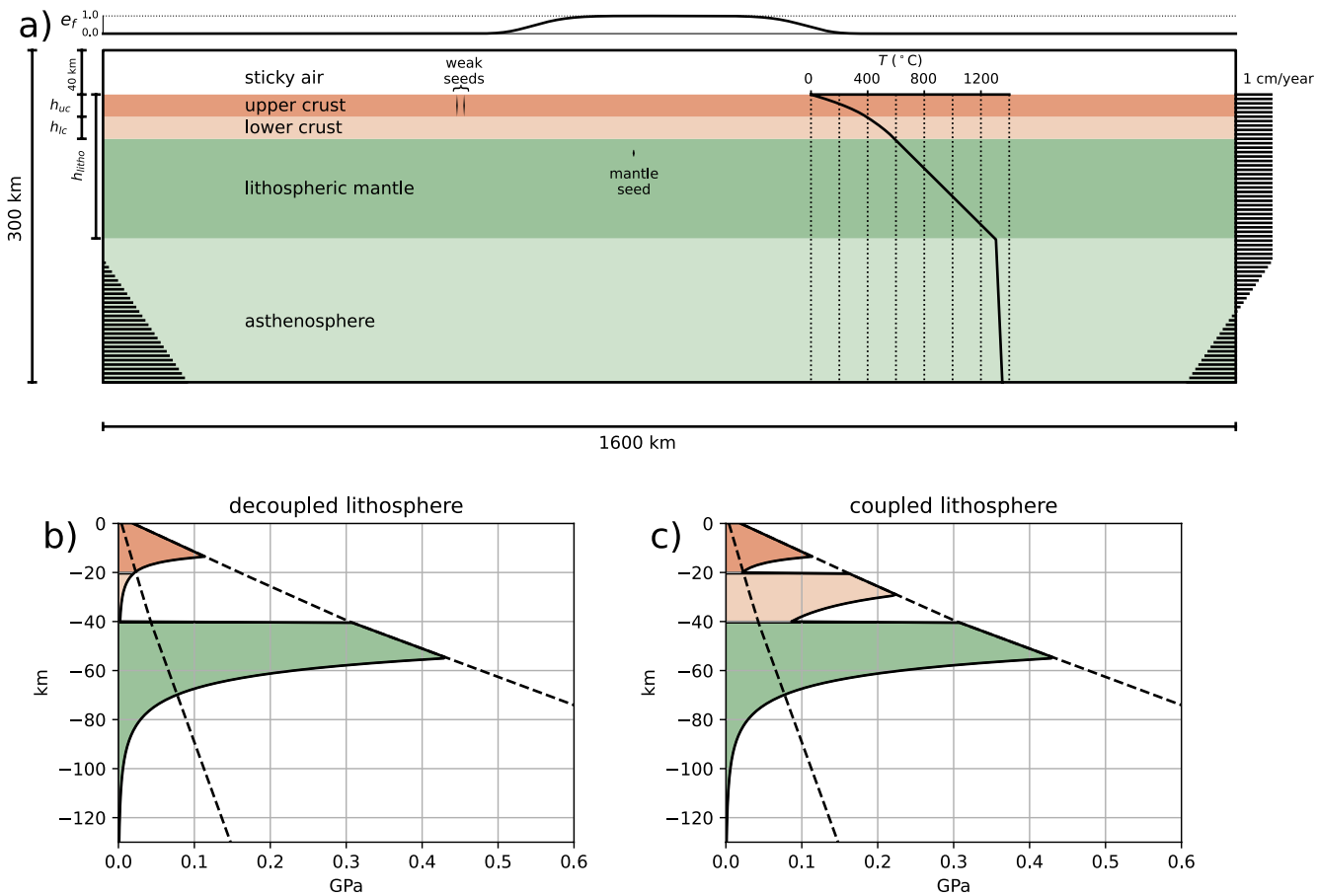

Figure 2. (a) Numerical model setup for the simulation of the lithospheric stretching. The thickness of the upper and lower crust is equal $h_{uc} = h_{lc} = 20$ km and the thickness of the lithosphere is $h_{litho} = 130$ km. The series of horizontal black lines on the left and right boundaries of the model indicate the boundary condition adopted for the velocity field. The upper curve indicates the denudation function e_f adopted, indicating that the maximum denudation occurs in the center of the domain, decreasing to the borders. Details about the function e_f are indicated in the text. The small mark close to the center of the lithospheric mantle is the mantle seed, necessary to localize the lithospheric stretching in the center of the domain. This mantle seed has a constant initial strain of 1.0 in all scenarios. Additionally, two vertical weak seeds were introduced in the upper crust in some of numerical experiments at $x = 460$ km and $x = 470$ km. (b–c) Yield strength envelope for the two reference numerical scenarios. The difference between the two scenarios is the scale factor C for the lower crust: $C = 1$ for decoupled lithosphere and $C = 40$ for coupled lithosphere. The dashed lines represent the plastic yield criterion for the maximum and minimum internal angle of friction ϕ and internal cohesion c_0 adopted in this work. In these diagrams, the viscous stress was calculated assuming that $\dot{\varepsilon}_{II} = 10^{-15}$ s^{-1}.

The sublithospheric temperature follows an adiabatic increase up to the bottom of the model:

$$T = T_p \exp(g\alpha z / c_p) \tag{10}$$

where $T_p = 1262$°C is the potential temperature for the mantle. Additionally, the temperature at all the boundaries was fixed during all numerical simulations, with the nodes of the model in the air maintained at 0°C.

To avoid a symmetric, laterally homogeneous model, we introduced a random perturbation of the initial strain in each finite element of the model (e.g., Brune et al., 2014). This random perturbation follows a normal distribution in which the mean initial strain is 0.2 with a standard deviation of ≈0.08. Additionally, to ensure the nucleation of rifting at the center of the numerical domain, we introduced a weak seed (e.g., Huismans & Beaumont, 2003) in the lithospheric mantle with a higher initial strain (Figure 2a). Other two weak seeds were introduced in the upper crust in some numerical experiments to represent the preexistence of crustal weakness before the lithospheric stretching (Figure 2a).

The numerical scenarios are classified into two main groups, named as "coupled lithosphere" and "decoupled lithosphere" (Figures 2b and 2c) where the only difference between them is the scale factor, C, for the lower crust viscosity: in the decoupled model $C = 1$, while in the coupled model $C = 40$, with a quartz flow law. This

means that for $C = 40$ this layer is 40 times more viscous at the same temperature, pressure, and strain rate regime compared with $C = 1$. The use of these nomenclatures represents an oversimplification, because both scenarios present a certain degree of coupling between the upper crust and lithospheric mantle, and part of the stress can be vertically transmitted through the different layers depending on the stress and temperature state of the entire lithosphere. The value of $C = 40$ for the coupled lithosphere is compatible with the values used in previous works to simulate strong crust bonded to the lithospheric mantle (e.g., $C = 30$–100 in Huismans & Beaumont, 2014).

The denudation on the top of the model was simulated by the imposition of a prescribed erosion rate variable in space and time. Other procedures can be adopted, like the assumption of a diffusion equation or a power law equation to simulate surface processes (e.g., Andrés-Martínez et al., 2019) or coupling with LEM codes (e.g., Beucher & Huismans, 2020). Here, we adopted the prescribed erosion rate to have control on the timing and extent of the erosion, facilitating the comparison of the different numerical scenarios with the same amount of escarpment retreat. Additionally, the surface processes adopted in the present work were limited to erosion of the continental margin, neglecting the influence of the sedimentary load on the marginal basin. Therefore, with this approach, we could isolate the effect of the erosional unloading on the strain pattern of the continental lithosphere. One additional scenario is presented in the Supporting Information where the sedimentation was also taking into account and the results are discussed in Section 4.2.

In each time step for the surface processes, the land/air interface is determined based on the limit between the "sticky air" and "land" particles. Erosion is applied in this interface based on the imposed denudation rate. Once a new level for the interface is obtained, all "land" particles above the interface are transformed to a "sticky air" particle.

The rate of erosion $\dot{e} = \dot{e}(x, t)$ is given by the following expression:

$$\dot{e} = k_{sp} e_f(x) c_f(t) \tag{11}$$

where e_f is a spatial control on denudation, given by

$$e_f(x) = \exp\left(-\frac{(x - x_c)^6}{x_\sigma^6}\right) \tag{12}$$

with x_σ controlling the spatial extent of the denudation from the center of the model at position $x = x_c$, while c_f is a climate function that rescales the magnitude of the denudation rate through time. The values of the different parameters of the surface processes are indicated in Table 2. The denudation rate $\dot{e}$ is only active if the topography h is above sea level h_{sl}. For the points at the surface below the sea level ($h < h_{sl}$), no surface processes were imposed. The values of k_{sp} and x_σ were chosen so that the denudation rate along the escarpment at the end of the numerical simulation was between 10 and 40 m/Myr, compatible to the long-term denudation rate observed on the Serra do Mar escarpment in southern Brazil (Salgado et al., 2014).

We adopted two types of climate scenarios: one reference model without erosion, where $c_f = 0$, and another one in which the denudation starts only 25 Myr after the onset of the lithospheric stretching:

$$c_f = \begin{cases} 0, & \text{if } t < 25 \text{ Myr} \\ 1, & \text{if } t \geq 25 \text{ Myr} \end{cases} \tag{13}$$

With these two climate scenarios, we try to evaluate the impact of the denudation on the postrift evolution of divergent margins. In these cases, both models present the same behavior until $t = 25$ Myr. After this moment, we can compare the impact of denudation on the lithospheric deformation in comparison with the reference model, that is, without erosion. This delay between the rifting phase and the onset of denudation in the numerical simulations reflects the denudation history observed along the marginal escarpments in southeastern Brazil. Thermochronological data (Gallagher & Brown, 1999) indicate that the first major increase in denudation rate in southeastern Brazilian margin occurred around the end of the Albian, nearly 20–30 Myr after the onset of rifting. The Santos Basin experienced a major increase in deposition of siliciclastic sediments during the Late Cretaceous (Gallagher & Brown, 1999) forming the Santos and Juréia Formations (Assine et al., 2008), reaching a thickness

of more than 3 km (Moreira et al., 2007). By initiating denudation only at the end of the rifting phase, we are directly able to test the influence of rifted margin erosion on intracratonal tectonic events.

3. Modeling Results

3.1. Thermomechanical Models Without Surface Processes

First, we present the results of the reference models, where no erosion is applied to the model and only one weak seed in the center of the model domain is used to nucleate the rifting process. In the reference decoupled scenario, the lower crust flows laterally during lithospheric stretching, while the upper crust is thinned essentially by a series of frictional-plastic shear zones (Figure 3a and Movie S1). This occurs because the lower crust is mainly in the viscous regime while the upper crust is in the plastic (brittle) regime. In this scenario, the continental breakup occurs at ≈25 Myr after the onset of lithospheric extension, resulting in a broad region with thinned crust, nearly 400 km wide when both conjugate margins are combined. On the other hand, in the reference coupled scenario, the lower crust is mainly in the plastic regime, and the stretching and thinning of the crust are essentially accommodated by extensional shear zones (Figure 3b and Movie S2). In this case, the zone of lithospheric thinning is narrower, resulting in a stretched continental crust zone of nearly 250 km (Figure 3b), with the continental breakup at ≈16 Myr. One important difference between these two scenarios is that in the decoupled model, the upper crust shear zones sole out in the lower crust, whereas in the coupled model the crust is mostly brittle and the shear zones extend into the upper mantle. In both reference scenarios, during the first ∼6 Myr, the strain rate is distributed throughout the lithosphere and starts to localize in the center of the model only after this period and the thinning of the lithospheric mantle occurs mainly between 6 and 18 Myr.

The strain rate decreases a few orders of magnitude in both conjugate margins after the breakup (Figure 4 and Movies S3 and S4). The magnitude of the strain rate along the frictional-plastic shear zones in the upper crust decreases through time, clearly observed in the decoupled scenario (Figure 4, 25.4–42.3 Myr). Additionally, due to the low viscosity of the lower crust in the decoupled scenario, even after the lithospheric breakup, the lower crust continues to flow during the postrift phase (Figure 4a), an aspect not observed in the coupled scenario (Figure 4b).

3.2. Thermomechanical Models With Surface Processes

In the scenario with the imposed erosion starting 25 Myr after the onset of the lithospheric stretching, the crustal unloading perturbs the stress state in the lithosphere (Figure 5b and Movie S5). The erosion concentrated mainly along the continental margins creates flexural stresses not only under the eroded portion of the margin but also in adjacent domains. For the decoupled scenario, the erosion induces regional uplift, creating a flexural bending of the crust with downward concavity. Due to the decoupled behavior of the lithosphere in this scenario, the upper crust and the lithospheric mantle behave as two plates separated by a low-viscosity lower crust. In this case, the stresses induced by erosional unloading are concentrated in the crust and are not efficiently transmitted to the lithospheric mantle. The erosion of the coastal escarpment and its progressive retreat toward the continent induces the bending of the crust with downward concavity, creating extension at the upper portion of the crust, accommodated by high-angle frictional-plastic shear zones, observed not only in the region under erosion but also in the offshore domain and in the continental interior (Figure 6a and letters F in Figures 5b and 5d). At the middle of the upper crust, it is possible to observe the flexural neutral surface (Figure 6a and NS in Figure 5b), marked by extremely low strain rates. Below this surface, the flexural compression in the crust is accommodated by viscous deformation.

On the other hand, the erosion of the margin in the coupled scenario induces a different stress pattern in the lithosphere (Figures 5d, 6b, and Figure S3 in Supporting Information S1 and Movie S6). Due to the partial coupling of the crust with the lithospheric mantle, the flexural rigidity of the lithosphere increases significantly (Burov & Diament, 1995). As a consequence, the wavelength of the flexural bending increases and the curvature of the lithosphere decreases, resulting in flexural stresses with smaller magnitudes in the upper crust. In this scenario, the brittle deformation in the continental interior is negligible, and postrift tectonism occurs essentially in the coastal plain and in the proximal offshore domain (Figures 5d and 6b).

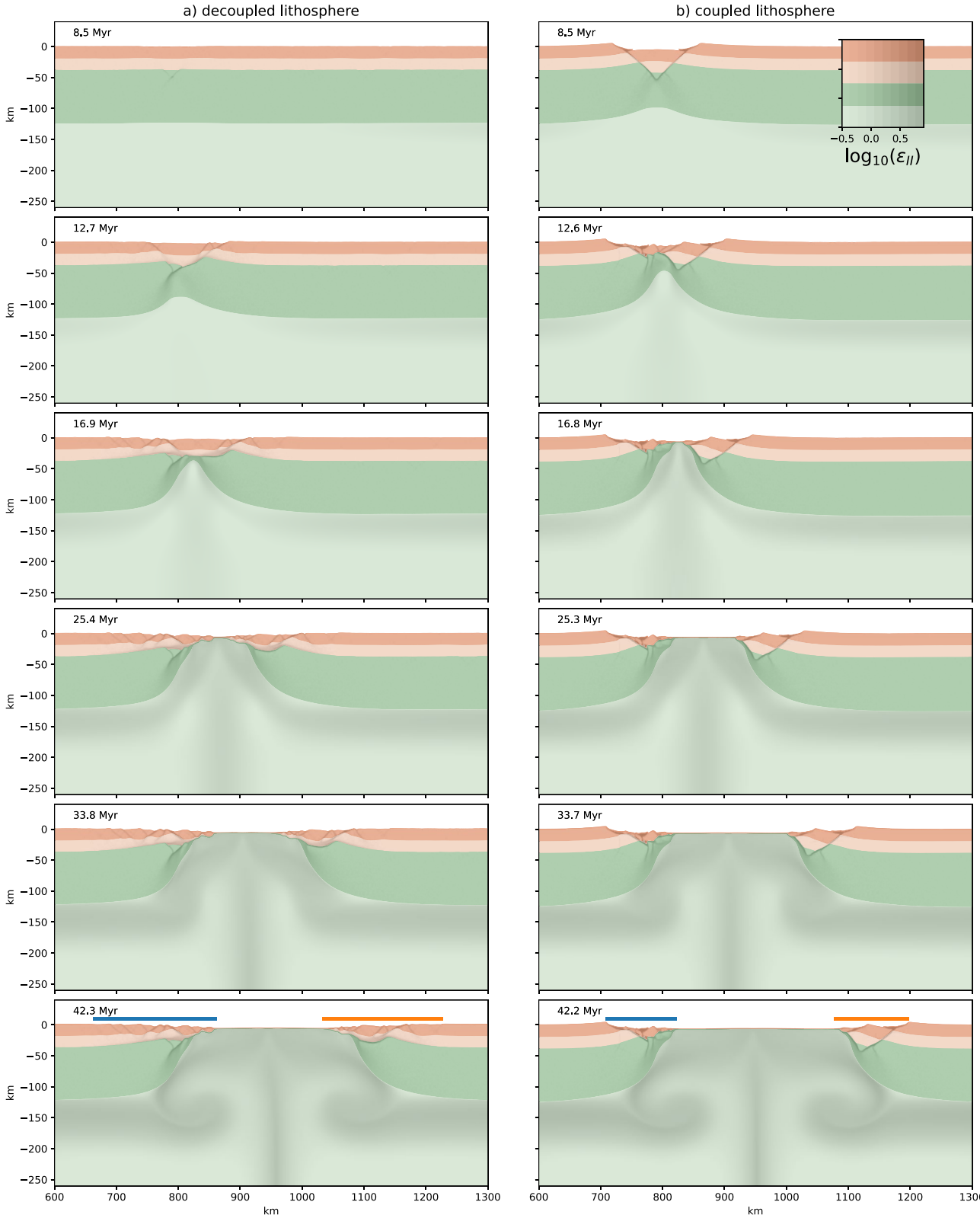

Figure 3. Evolution of the reference numerical scenarios with decoupled lithosphere (a) and coupled lithosphere (b), with $C = 1$ and 40 for the lower crust, respectively. Both scenarios are without surface processes. Dark and light orange represent the upper and lower crust, respectively, while dark and light green represent lithospheric and sublithospheric mantle, respectively. Shades of gray indicate the magnitude of cumulative strain. The blue and orange bars indicate the width of the extended continental crust in both conjugate margins. See the model evolutions in Movies S1 and S2.

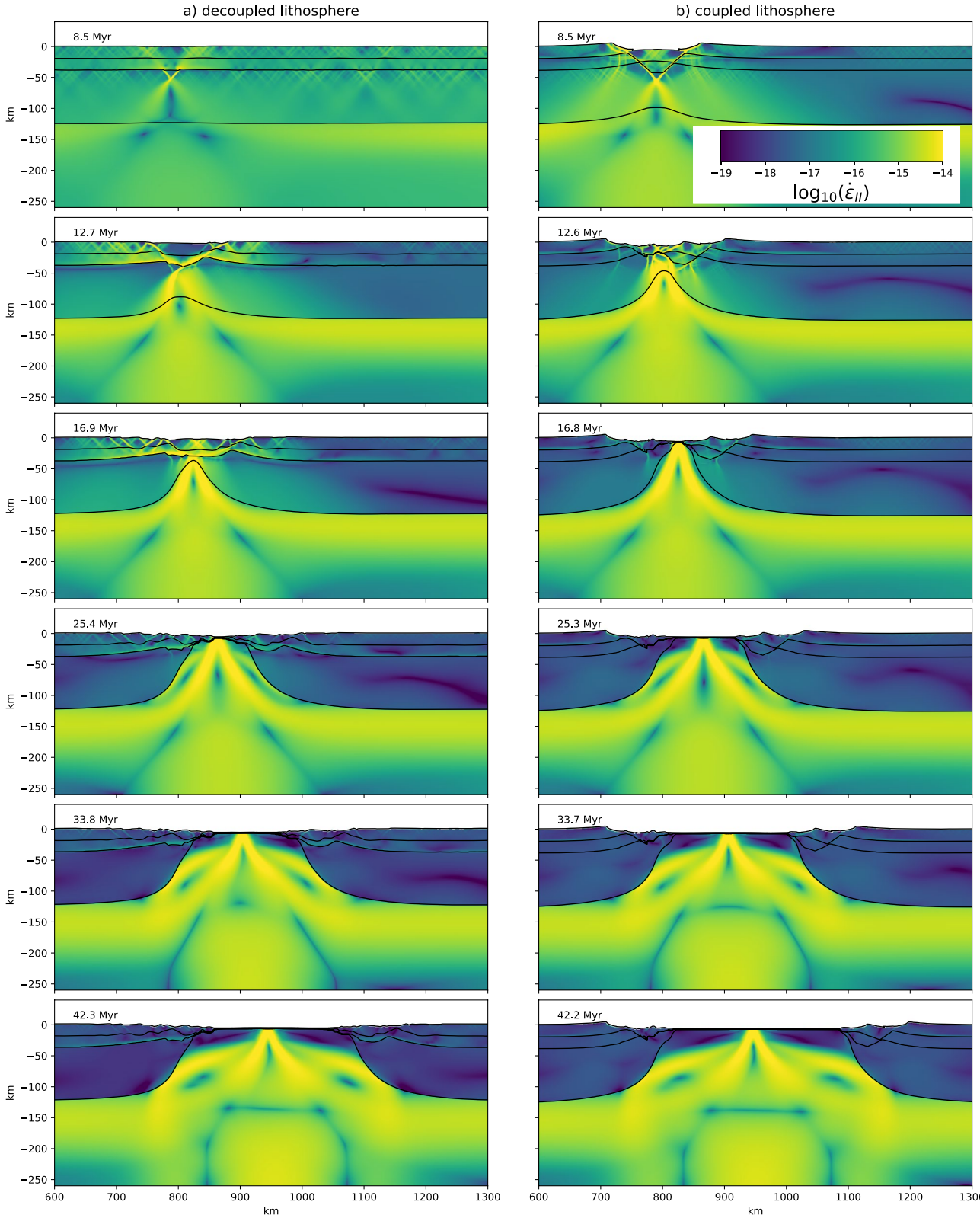

Figure 4. Evolution of the strain rate for the reference scenarios with decoupled lithosphere (a) and coupled lithosphere (b), with $C = 1$ and 40 for the lower crust, respectively. The strain rate $\dot{\epsilon}_{II}$ is in 1/s. Black lines indicates the boundaries between the different compositions. See the model evolutions in Movies S3 and S4.

10.1029/2021TC006808

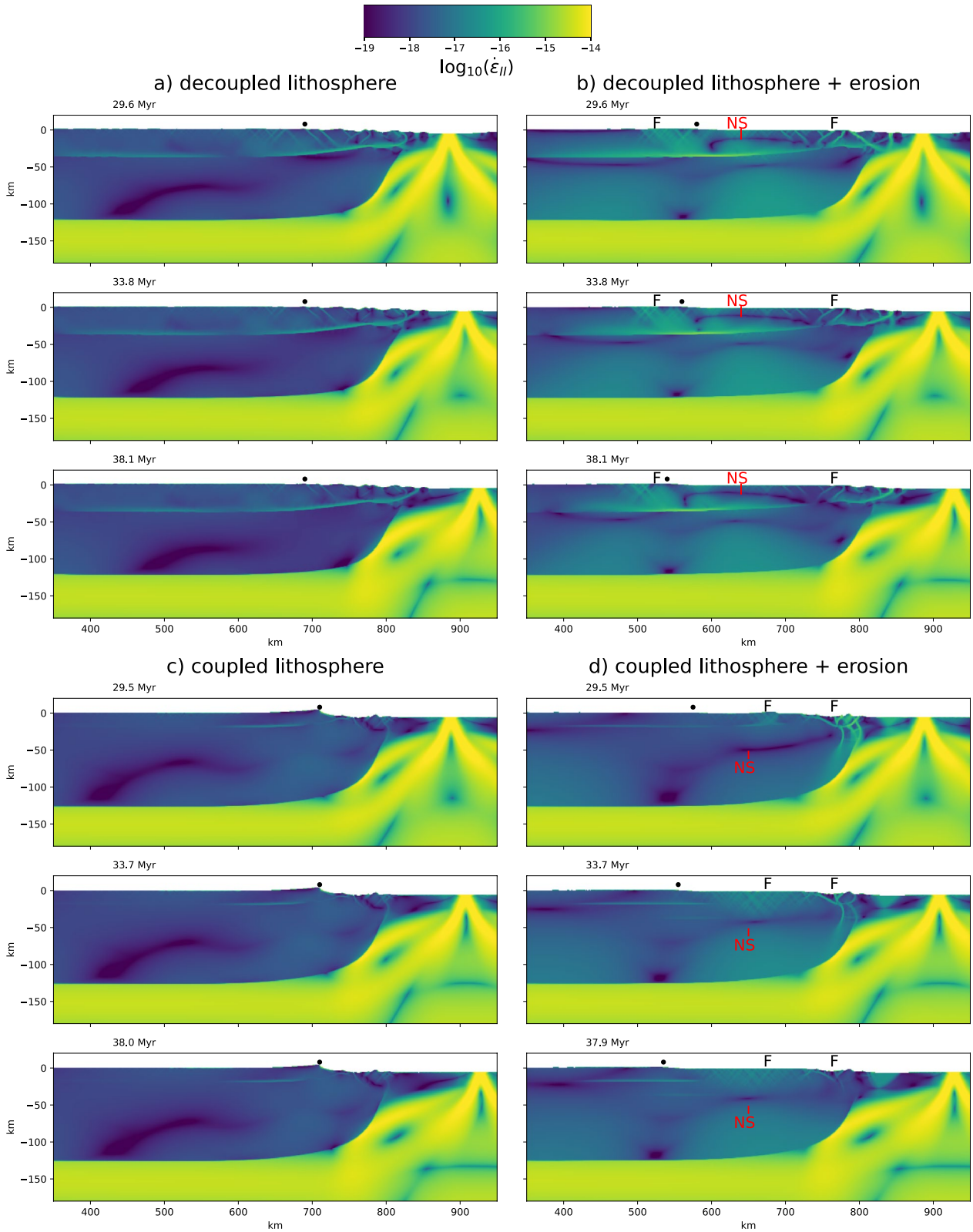

Figure 5. Comparison of the strain rate field for the scenarios with and without erosion for the decoupled (a–b) and coupled (c–d) lithosphere ($C = 1$ and $C = 40$ for the lower crust, respectively). The strain rate $\dot{\varepsilon}_{II}$ is in 1/s. The letters F indicate zones in the upper crust with active frictional-plastic shear zones similar to faults and NS indicate the flexural neutral surface. The black dots above the surface indicate the approximate position of the escarpment in the different scenarios. See the evolution of the models with erosion (b and d) in Movies S5 and S6.

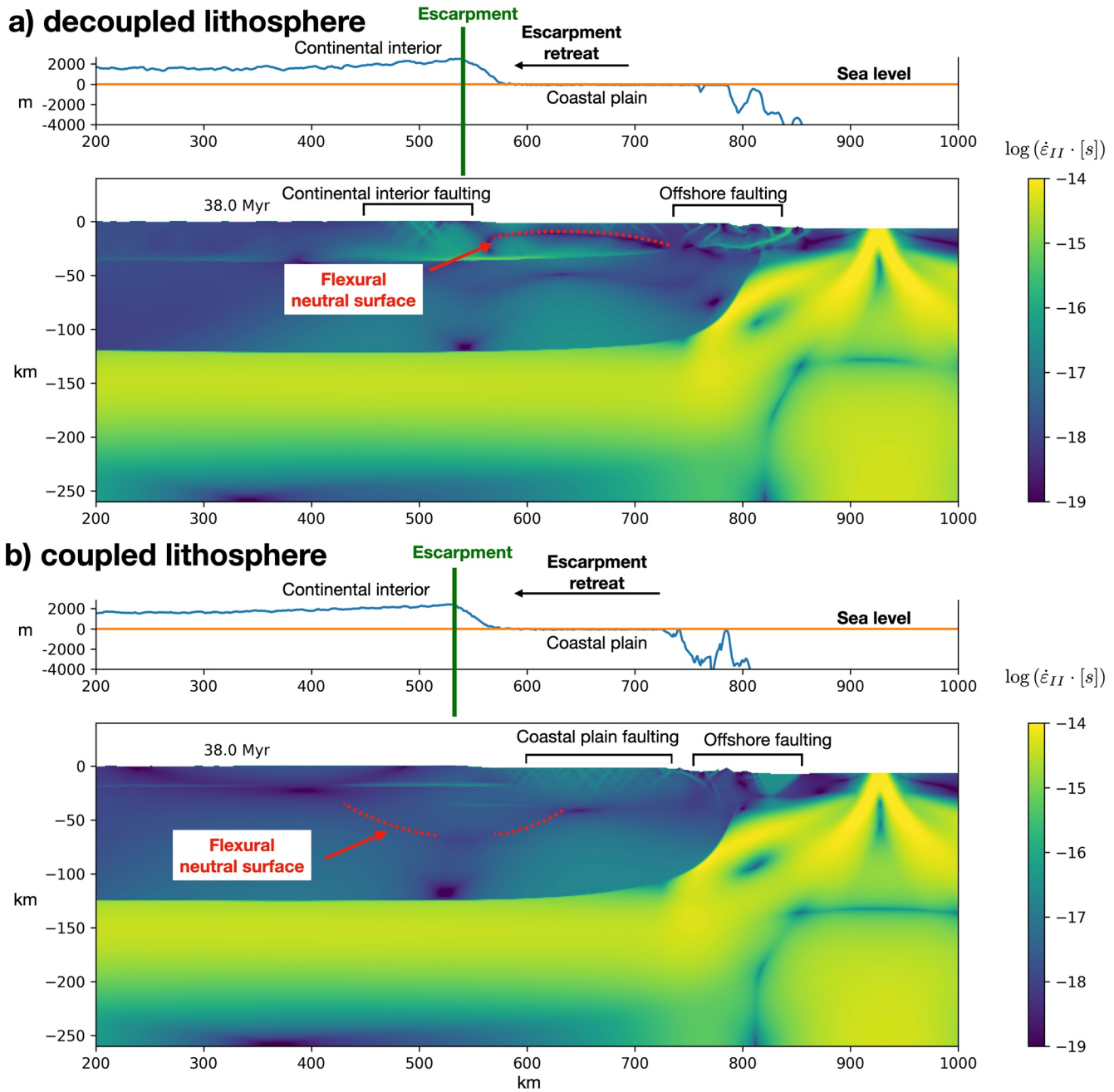

Figure 6. Topographic profile and strain rate pattern in the lithosphere for the (a) decoupled scenario and (b) coupled scenario ($C = 1$ and $C = 40$ for the lower crust, respectively) and with erosion. The upper panel presents the topographic profile in blue, indicating the position of the escarpment separating the coastal plain from the continental interior. The flexural neutral surface is shown as a red dashed line in the lower panel.

3.3. Thermomechanical Models With the Preexistence of Weakness in the Upper Crust

For our final set of numerical experiments, we considered scenarios where the upper crust has two preexisting weaknesses, as shown in Figure 2a. The initial position of these two upper crustal weaknesses was chosen as $x = 460$ and 470 km. For the decoupled scenarios with surface erosion and crustal weakness, the postrift tectonism induced in the continental interior is concentrated close to the weak seed and, consequently, produces larger strain rates (Figure 7, right column) than in the scenario without crustal weakness (Figure 7, left column). Due to the concentrated strain in the region close to the crustal weakness, increased frictional-plastic strain is evident at the surface of the model (Figure 8, right column) generating an initial graben during the onset of lithospheric

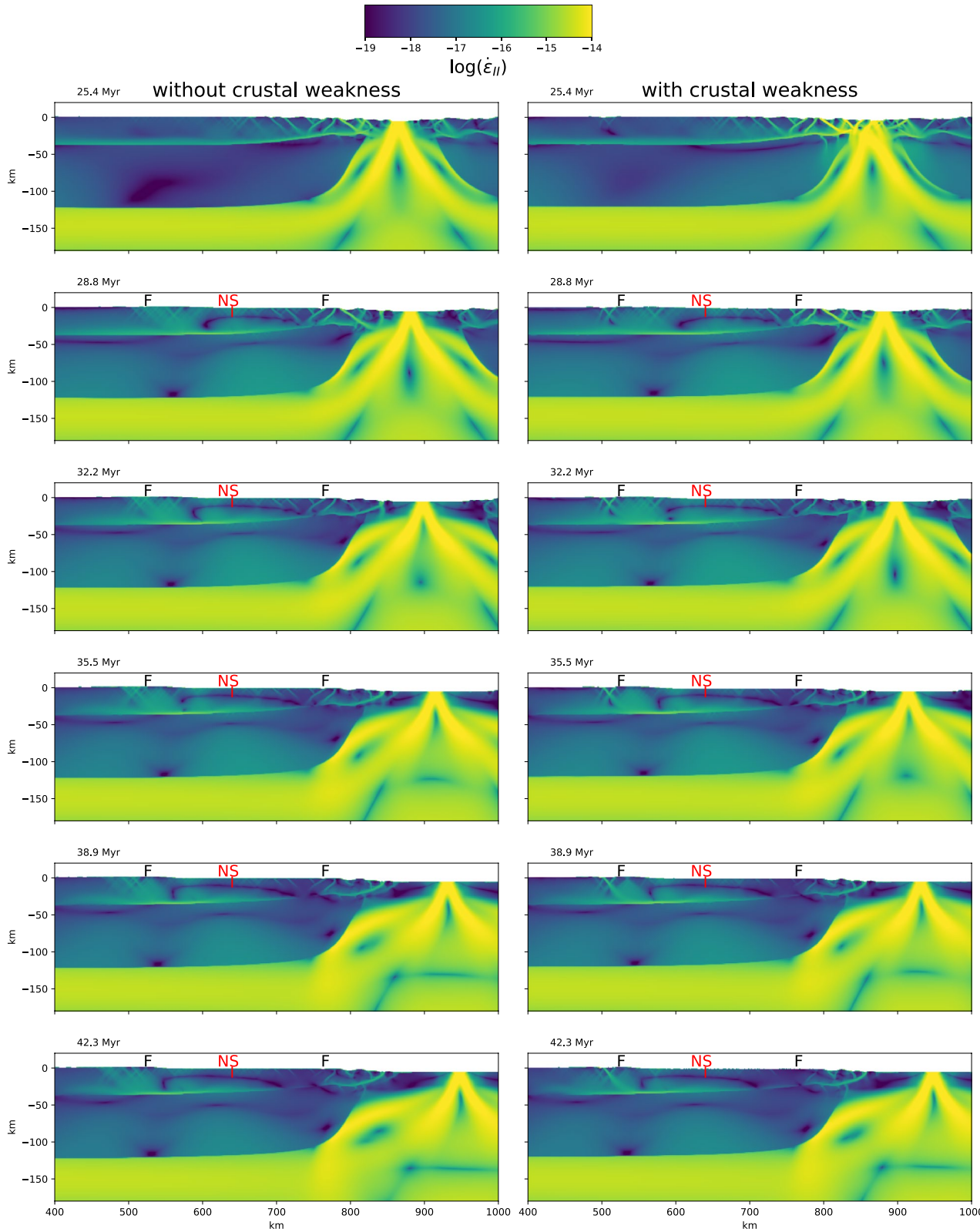

Figure 7. Comparison of the strain rate field for the scenarios with and without weak seeds in the upper crust for the decoupled lithosphere ($C = 1$). Both models have erosion acting on the surface. The strain rate $\dot{\varepsilon}_{II}$ is in units of 1/s. The letters F indicate zones in the upper crust with active frictional-plastic deformation and NS indicate the flexural neutral surface. Both axes are in kilometers.

10.1029/2021TC006808

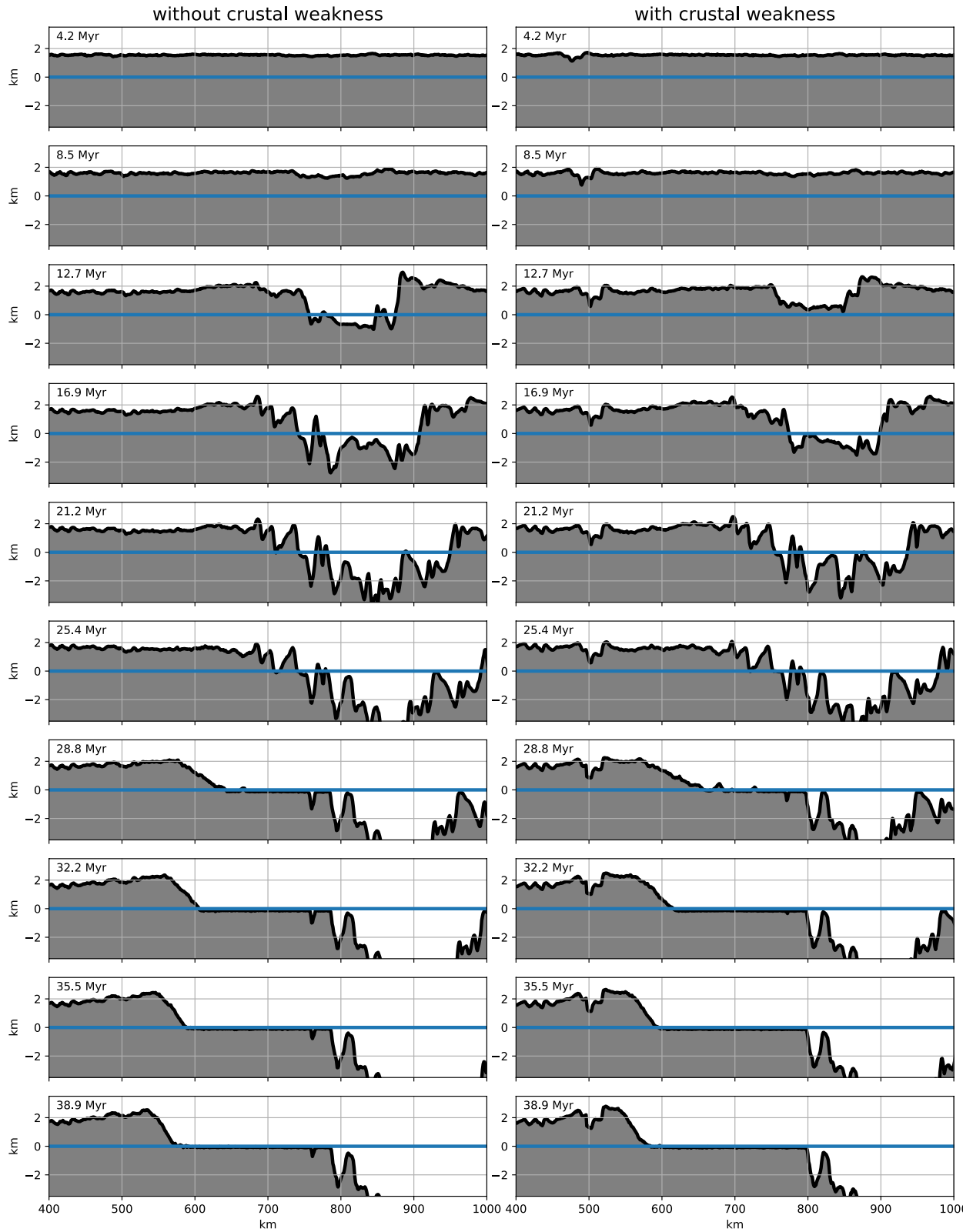

Figure 8. Topographic evolution for the scenarios shown in Figure 7. The blue line represents the sea level. Between $x = 475$ and 525 km, a graben develops in the scenario with crustal weakness.

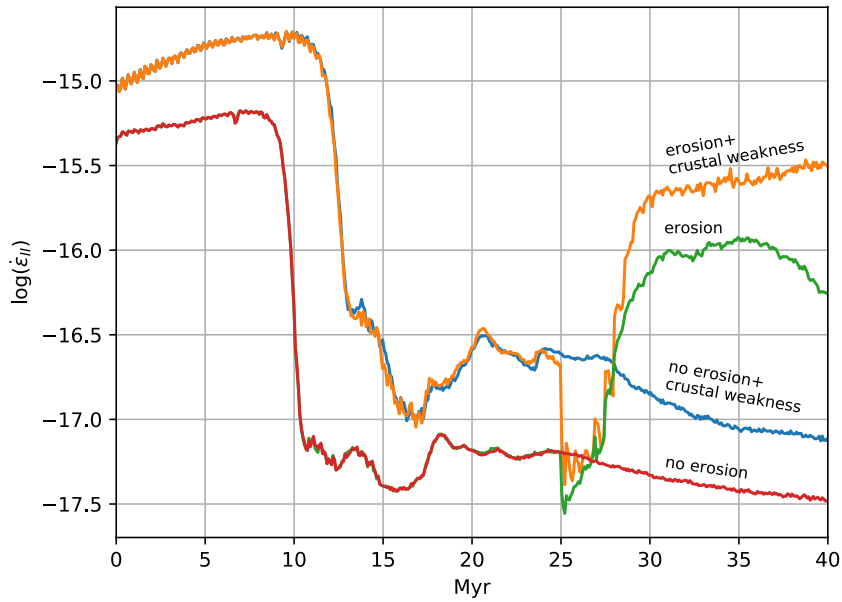

Figure 9. Maximum strain rate in the upper crust along the interval between $x = 500$ and 600 km for four scenarios. The erosion of the continent starts at 25 Myr in the scenarios with erosion (green and orange curves).

stretching in the first 8 Myr of simulation that is reactivated during the denudation phase of the margin. This graben is not formed in the scenario without the preexistence of the upper crustal weakness, where the postrifting frictional-plastic deformation is more diffuse in the continental interior (Figure 8, left column).

In all of our numerical experiments, the maximum strain rate in the upper crust in the continental interior occurs during the initial stage of lithospheric stretching ($\lesssim$10 Myr), where the strain is distributed through the entire domain (Figure 9). After this time interval, the strain rate drops nearly 2 orders of magnitude in the continental interior due to the localization of the stretching in the center of the numerical domain.

The maximum strain rate increases slowly during the final stage of lithospheric stretching until ~25 Myr, a period marked by expressive thinning of the lithospheric mantle and concentration of the stretching in the continental crust. In the scenarios without erosion, the strain rate in the continental interior decreases almost monotonically after the end of the rifting phase and through all the postrift phase. However, in the scenarios with imposed erosion at $t = 25$ Myr, the maximum strain rate increases by more than 1 order of magnitude relative to the scenarios without erosion (Figure 9). When the erosion is applied in combination with the presence of weakness in the intracontinental upper crust, the maximum strain rate becomes more than 100 times larger than the one observed in the same scenario but without intracontinental crustal weakness and no erosion (Figure 9). Additionally, in the scenario with erosion and crustal weakness, the maximum strain rate after the onset of erosion at 25 Myr is of the same order as the maximum strain rate during the initial lithospheric stretching (<10 Myr). We also find that a higher magnitude of denudation results in higher deformation observed in the upper crust in the continental interior (Figure S1 in Supporting Information S1).

4. Discussion

4.1. The Mechanism for Postrift Tectonism Induced by Erosion

Based on analytical expressions assuming pure elasticity, it is well known that the uniform erosion of the crust can induce compressive stresses at the surface due to the elastic behavior of the rocks. The horizontal compressive stress σ_h at the surface is given by (Turcotte & Schubert, 2002)

$$\sigma_h = \left(\frac{1-2\nu}{1-\nu}\right)\rho_c g h_{erod}$$

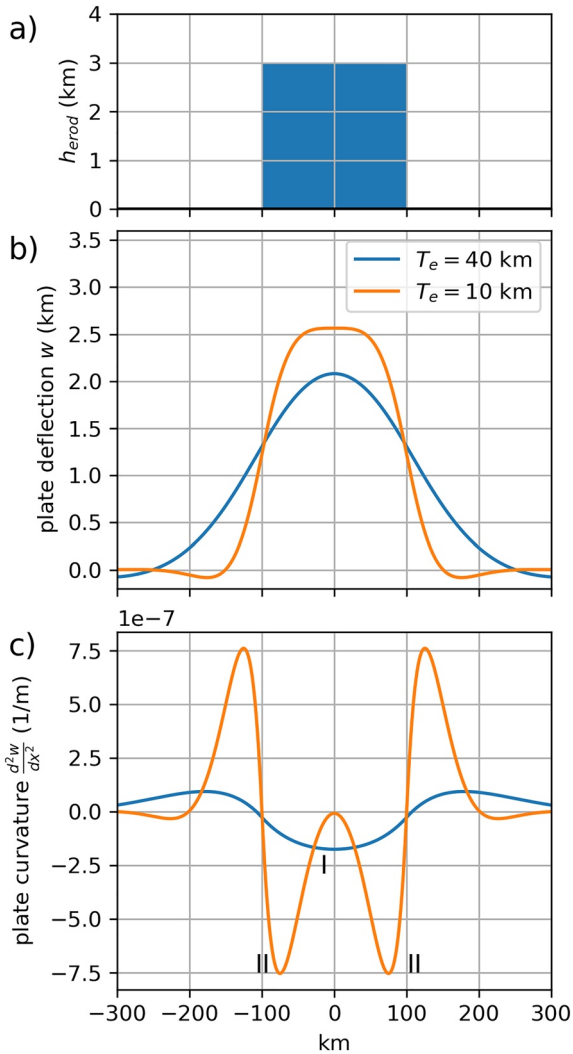

Figure 10. Analytical solution for the flexure of a thin elastic plate under a uniform load distributed in the interval between −100 and 100 km. (a) Thickness h_{erod} of the eroded crust, resulting in the unloading of the lithosphere. (b) Flexural response of the elastic plate for two different effective elastic thicknesses: T_e = 10 and 40 km. (c) Curvature of the plate for the two cases shown in (b). I and II indicate the locations of maximum curvature with downward concavity for T_e = 40 and 10 km, respectively.

where ν is the Poisson's ratio, ρ_c is the crust density, and h_{erod} is the thickness of the eroded layer. Assuming $\nu = 0.25$, $\rho_c = 2{,}700$ kg/m^3, $g = 10$ m/s^2, and $h_{erod} = 3$ km, the horizontal stress is $\sigma_h = 54$ MPa.

However, this expression is only valid if we consider the uniform erosion of a horizontal layer with constant thickness. If the erosion is localized and therefore geographically finite, flexural extensional stresses will be generated at the surface that can easily surpass the magnitude of compressive stresses obtained in the previous analytical solution. Assuming an elastic rheology, the magnitude of the horizontal stress σ_{xx} along the axis x generated by the bending of an elastic plate with effective elastic thickness T_e is given by (Turcotte & Schubert, 2002)

$$\sigma_{xx} = \frac{E}{1-\nu^2}\epsilon_{xx} = \frac{E}{1-\nu^2}\frac{T_e}{2}\frac{d^2w}{dx^2} \tag{14}$$

where E is the Young's modulus, ϵ_{xx} is the strain along the x axis, and d^2w/dx^2 is the curvature of the plate. In this expression, σ_{xx} is calculated at the surface of the plate at a distance $T_e/2$ from the flexural neutral surface. Assuming reasonable values ($d^2w/dx^2 \sim 10^{-7}$ to 10^{-6} m^{-1}) for the plate curvature due to flexural effects (Lavier & Steckler, 1997) and T_e = 20 km, the resulting extensional stresses are $\sigma_{xx} \approx$ 100–1,000 MPa. Obviously, this analysis is a simplification, assuming a perfect elastic plate, but demonstrates the importance of the flexural stresses relative to the stresses induced by erosive exhumation.

Keeping in mind the simplicity and limitation of the elastic plate approach, here we present a simplified analogous model for the thermomechanical model presented in the previous section, showing the physical explanation for the difference in the stress patterns obtained in the coupled and decoupled scenarios. Considering an infinite thin elastic plate with rigidity $D = ET_e^3/12(1-\nu^2)$ floating on an inviscid fluid with density ρ_m and under the load q uniformly distributed over the segment A–B of the plate, the deflection $w(x)$ of the plate at the point x, which is a distance a from A and a distance b from B is given by (Hetényi, 1946)

$$w(x) = \begin{cases} \dfrac{q}{2\rho_m g}\left(e^{-\lambda a}\cos\lambda a - e^{-\lambda b}\cos\lambda b\right), & \text{if } x \le A \\ \dfrac{q}{2\rho_m g}\left(2 - e^{-\lambda a}\cos\lambda a - e^{-\lambda b}\cos\lambda b\right), & \text{if } A < x < B \\ \dfrac{-q}{2\rho_m g}\left(e^{-\lambda a}\cos\lambda a - e^{-\lambda b}\cos\lambda b\right), & \text{if } B \le x \end{cases} \tag{15}$$

where $\lambda = \sqrt[4]{\rho_m g/4D}$.

Assuming that the load $q = \rho_c g h_{erod}$ is upward, representing the unloading due to the erosion of a layer of the crust with thickness h_{erod} = 3 km, density ρ_c = 2,700 kg/m^3, and width of 200 km (Figure 10a), the flexural response of the lithosphere depends on the flexural rigidity of the plate. Using Equation 15, for an effective elastic thickness T_e = 40 km, the long-wavelength upward movement of the plate occurs over a segment of the plate of nearly 500 km, while for a T_e = 10 km the upward movement occurs in a narrower region in a segment of nearly 300 km (Figure 10b). For these two cases, the maximum uplift coincides with the center of the (un)load.

However, the curvature of the plate d^2w/dx^2, which is proportional to the horizontal stress σ_{xx} (see Equation 14), presents different patterns for the locations of maxima and minima in these two cases (Figure 10c). For the case with T_e = 40 km, the maximum curvature with downward concavity (Figure 10c, symbol I), is in the center of the load, generating the maximum extension at the surface exactly under the eroded area. In the case with T_e = 10 km, the maximum curvature with downward concavity occurs close to the limits of the eroded area (Figure 10c,

symbols II), while in the center the concavity is close to zero. Therefore, in this case, the extension is maximum on the borders of the eroded area.

These flexural patterns are similar to what was observed in the thermomechanical scenarios of the previous section. The case with $T_e = 40$ km is compatible with the scenario with coupled lithosphere, where the unloading of the margin due to the escarpment erosion resulted in the development of structures similar to normal faults mainly in the coastal plain, the center of the unloading of the margin. On the other hand, the case with $T_e = 10$ km is similar to the scenario with decoupled lithosphere, where the erosion of the escarpment induced shear/faulting mainly in the continental interior and along the offshore margin previously stretched.

It is important to highlight that the effective elastic thickness used in the analogous experiments does not represent any physical layer in the interior of the lithosphere but represents an integrative contribution of the flexural rigidity of the crust and lithospheric mantle (see Burov & Diament, 1995, for a detailed analysis of the meaning of the effective elastic thickness in the continental lithosphere). For the scenario with decoupled lithosphere, the effective elastic thickness is essentially calculated based on the rigidity of the upper crust, with a negligible contribution of the lithospheric mantle. On the other hand, in the coupled lithosphere case, the effective elastic thickness combines the rigidity of the crust and the lithospheric mantle.

4.2. Comparison to Continental Divergent Margins

The two groups of scenarios tested in the present work, defined here as coupled and decoupled models for simplicity, resulted in different geometries for the stretched margin, mainly due to crustal strength dependency (e.g., Tetreault & Buiter, 2018). In the decoupled models, the domain of crustal thinning covers a region of ~400 km in which the zone where the crust is thinner than 15 km thick (defined as hyperextended by Pérez-Gussinyé et al., 2020), represents nearly half of this width. On the other hand, in the coupled models, the extension zone is nearly 250 km with hyperextended crust of less than 100 km. Here, we chose to increase the scale factor C for the lower crust to simulate the lithospheric coupling, but other approaches are possible which would give similar results, like the use of a different creep flow law for the lower crust (e.g., Brune et al., 2014) or the initial thermal structure of the lithosphere.

These two sets of numerical experiments presented here are rheologically compatible to the numerical scenarios of Type 2 presented by Pérez-Gussinyé et al. (2020). In both works, the initial crustal thickness is 40 km and the temperature at the base of the crust is close to 600°C. In these cases, the conjugate margins are asymmetric (although the degree of asymmetry is significantly different between the two works), with the width of the margins as a function of the strength of the lower crust.

Possibly, the degree of asymmetry of the conjugate margins in our work is smaller than the one obtained by Pérez-Gussinyé et al. (2020) due to differences in the choice of the material for the lower crust, thereby affecting the rheology of this layer. In fact, when Brune et al. (2017) adopted wet quartzite for the entire crust, resulting in a very weak rheology for the crust, they obtained wide and symmetric margins. Similarly, when the initial temperature at the base of the crust was increased from 600 to 700°C, using the rheology of wet anorthite, resulting in a decrease in the effective viscosity of the lower crust, Pérez-Gussinyé et al. (2020) obtained wide and symmetric margins.

Our experiments with coupled lithosphere are similar to the models Type 2a in Pérez-Gussinyé et al. (2020) representing scenarios with strong lower crust, resulting in asymmetric margins with large offset shear zones but with relatively narrow margins. This kind of coupled lithosphere was previously used to explain the continental rifting between Iberia and Newfoundland (Brune et al., 2017), reproduced in numerical scenarios with the rifting phase enduring for ~16 Myr and resulting in combined conjugate margins with ~230 km, similar to our numerical scenario presented in Figure 4b. On the other hand, our experiments with a decoupled lithosphere are compatible with the model Type 2b in Pérez-Gussinyé et al. (2020) representing scenarios with weak lower crust, resulting in asymmetric margins with small offset shear zones but with wide conjugate margins, with hundreds of kilometers wide. Similarly, a weak lower crust was proposed to explain the development of the hyperextended crust between Brazil–Angola conjugate margins (Brune et al., 2017), classifying the rifting process into three phases: (a) simultaneous faulting, distributed over hundreds of kilometers and enduring for ~17 Myr; (b) rift migration phase that amplifies the asymmetry between the conjugate margins and persists for ~18 Myr; and (c) finally resulting in continental breakup, with combined conjugate margins widths greater than 400 km. This temporal evolution

and spatial extent of the rifting process is compatible with the decoupled scenario presented in Figure 4a. One example of this kind of conjugate margins is the Kwanza–Campos/Espírito Santo margins between Africa and Brazil, where the margins can exceed 200 km wide (Brune et al., 2014). Southward, in the Santos, the width of the Brazilian margin can reach more than 500 km. We propose that the development of this anomalous stretched margin in southeastern Brazil of more than 400 km is induced by the low degree of coupling between the upper crust and lithospheric mantle during the development of the rifting.

In addition to this singular wide extended margin, the adjacent onshore southeastern Brazilian margin presents a peculiar double pattern of escarpments parallel to the margin, the Serra da Mantiqueira and Serra do Mar escarpments (Figure 1a), limiting the sedimentary basins of the CRSB. We propose that the development of the CRSB can be explained by local stresses induced by the flexural response of the lithosphere to the unloading of the margin, as previously proposed by Silva and Sacek (2019). Here, we expand this analysis taking into account a thermomechanical numerical model with a rheology that combines brittle failure and creep flow, simulating the evolution of the margin since the onset of the lithospheric stretching.

In the present numerical experiments, we were able to reproduce the development of frictional-plastic deformation similar to normal faults and the formation of a graben in the continental interior compatible with the CRSB between the Serra do Mar and Serra da Mantiqueira escarpments. This was possible due to the combination of three different factors:

1. The decoupling of the crust and the lithospheric mantle, favoring the development of a hyperextended margin as observed in the southeastern Brazilian margin (Karner, 2000; Zalán et al., 2011) with the continent–ocean boundary hundreds of kilometers far from the coast (Figure 1a). As exemplified by the analytical solution of the thin elastic plate shown in Figure 10, the plate curvature will be amplified due to the low flexural rigidity in the decoupled lithosphere.
2. Postrift exhumation due to erosion of the margin with a magnitude between 3 and 4 km (Cogné et al., 2011). Additionally, assuming that the initial escarpment was formed along the offshore Cretaceous hinge line (Figure 1a), the total escarpment retreat can be larger than 100 km since the continental breakup. Furthermore, thermochronological data (Cogné et al., 2011; Hiruma et al., 2010) indicate that pulses of erosional exhumation during the Late Cretaceous preceded the filling of the interior basins of the CRSB. The load of the sedimentary layers deposited in the offshore Santos Basin induced an additional flexural influence in the continent, creating an adjacent flexural bulge that could amplify the extensional stresses created by the erosional unloading of the continental margin (see Figure S2 in Supporting Information S1). However, the sedimentary load represents a secondary effect on the strain pattern of the continental interior. In fact, the main differences between the scenarios with and without sedimentation occur close to the offshore domain, in the stretched crust, with amplified strain rate in the scenario with sedimentation.
3. Preexistence of crustal weaknesses along the continental margin. The formation of grabens in zones of weaknesses is well known (Dunbar & Sawyer, 1988). Also, the crystallographic lattice preferred orientation of olivine crystals in the lithospheric mantle has been related to preexisting weakness zones and rifted margin formation (Tommasi & Vauchez, 2001, 2015). In particular, the CRSB evolved on the shear zones of the Precambrian rocks of the Ribeira Belt (Trouw et al., 2000), nearly parallel to the present margin.

It is important to highlight that in our numerical simulations, the graben generated in the continental interior was initially formed during the initial lithospheric stretching in the first ~8 Myr of simulation and reactivated during the postrift pulse of erosive exhumation of the margin. There is no clear geological evidence that the CRSB was tectonically active during the formation of the South Atlantic margins, although Cogné et al. (2013) argue that the basement reactivated during the Late Cretaceous before the initial sedimentary infilling of the basins in the CRSB. In the conjugate margin, onshore tectonism occurred at the time of rifting of South Atlantic due to reactivation of Neoproterozoic shear zones of the Kaoko Belt (Salomon et al., 2015), although the precise time of reactivation is still uncertain. Salomon et al. (2015) argue that this reactivation did not influence the main rift and was a side effect of rifting.

The numerical experiments presented here only can explain the initial stage of tectonism that created the series of grabens in the CRSB. Our two-dimensional thermomechanical model is not able to take into account other tectonic forces that modified the geometry of the basins, including the influence of the Andean orogeny and the

obliquity of the CRSB relative to the evolving stress state of the lithosphere, and only three-dimensional codes can appropriately simulate these components.

5. Conclusions

This work evaluated the effects of erosion and lithospheric stretching on the postrift margin evolution using an integrated coupled model of Earth's interior dynamics and surface processes in extensional settings. In scenarios where the lower crust had relatively lower viscosity than the upper crust, resulting in a decoupled lithosphere and a low effective elastic thickness, a hyperextended rifted margin is obtained. In this scenario, when denudation of the margin is present, maximum strain occurred at the limits of the eroded region as a result of the flexural response of the lithosphere. For scenarios where the lower crust had relatively high viscosity resulting in a coupled lithosphere, the maximum strain occurred precisely beneath the denudation region. Hence, very little strain occurred on the continental interior. These results suggest that the occurrence of postrift tectonism in the hinterland is favored when the margin has a decoupled lithosphere and high magnitude of denudation. The numerical results also indicate that the preexistence of a shear zone in the continent favors tectonism.

The southeastern Brazilian margin is unique in the world, featuring a hyperextended lithosphere in which the distance from the coastline to the continent–ocean boundary exceeds 500 km. Based on numerical experiments results, the hyperextension requires a decoupled lithosphere. This factor was also of primary importance to generate tectonism on the interior of the continent.

Appendix A: Left and Right Boundary Conditions for Velocity

The horizontal velocity field along the left and right borders of the domain presents two layers (Figure 2):

1. constant velocity with depth at $0 \leq z < h_c$;
2. linearly variable velocity with depth at $h_c \leq z \leq h_c + h_a$,

where z is the vertical axis with origin at the Earth's surface and pointing downward, $h_c = 150$ km is the thickness of the upper layer with constant velocity, corresponding to the lithosphere $h_{litho} = 130$ km and part of the asthenosphere, and $h_a = 110$ km corresponds to the remaining asthenospheric portion of the model until the bottom of the model, where the horizontal velocity at the borders of the model varies linearly with depth. Therefore, the sum $h_c + h_a$ represents the total thickness of the model without the "sticky air" layer.

Considering that the reference frame is fixed with the left portion of the model and that the right portion of the lithosphere is moving rightward with a velocity of v_{rift}, and ensuring conservation of mass, the horizontal components of the velocity on the left and right side of the domain, respectively v_L and v_R, are

$$v_L(z) = \begin{cases} 0, & \text{if } 0 \leq z < h_c \\ v_b \dfrac{z - h_c}{h_a}, & \text{if } h_c \leq z \leq h_c + h_a \end{cases} \tag{A1}$$

$$v_R(z) = \begin{cases} v_{rift}, & \text{if } 0 \leq z < h_c \\ -v_b \dfrac{z - h_c}{h_a} + v_{rift}, & \text{if } h_c \leq z \leq h_c + h_a \end{cases} \tag{A2}$$

where

$$v_b = v_{rift} \frac{h_c + h_a}{h_a} \tag{A3}$$

so that

$$\int_0^{h_c+h_a} v_L dz = \int_0^{h_c+h_a} v_R dz = \frac{v_b h_a}{2}. \quad \text{(A4)}$$

In Equation A4, material flows in along the left boundary, while along the right boundary, the net flow is outward, and since mass conservation is assumed, the sum of the integrals over the boundary is zero. Additionally, the horizontal velocity at the left and right borders of the model above the Earth's surface, in the "sticky air" layer, was maintained at null throughout the numerical simulation. The tangential velocities on all boundaries were left free.

Conflict of Interest

The authors declare no conflicts of interest relevant to this study.

Data Availability Statement

The numerical code is available through GitHub repository (https://github.com/ggciag/mandyoc). The version used and simulations input files are archived in Zenodo https://doi.org/10.5281/zenodo.5083424.

Acknowledgments
This work was supported by FAPESP PhD scholarship grant 2017/10554-4 to R. M. Silva. Data modeling made use of the computing facilities of the Laboratory of Tectonophysics II -Numerical Modeling (IAG/USP) and HPC resource funded by FAPESP (project 2017/24870-5) and Petrobras (project 2017/00461-9). We thank two anonymous reviewers for their constructive comments which improved the quality and clarity of the manuscript.

References

Andrés-Martínez, M., Pérez-Gussinyé, M., Armitage, J., & Morgan, J. P. (2019). Thermomechanical implications of sediment transport for the architecture and evolution of continental rifts and margins. *Tectonics*, *38*, 641–665. https://doi.org/10.1029/2018TC005346

Artemieva, I. M. (2006). Global 1° × 1° thermal model TC1 for the continental lithosphere: Implications for lithosphere secular evolution. *Tectonophysics*, *416*(1–4), 245–277. https://doi.org/10.1016/j.tecto.2005.11.022

Assine, M. L., Corrêa, F. S., & Chang, H. K. (2008). Migração de depocentros na Bacia de Santos: Importância na exploração de hidrocarbonetos. *Revista Brasileira de Geociências*, *38*(2 Suppl), 111–127. https://doi.org/10.25249/0375-7536.2008382s111127

Assumpção, M., Bianchi, M., Julià, J., Dias, F. L., França, G. S., Nascimento, R., et al. (2013). Crustal thickness map of Brazil: Data compilation and main features. *Journal of South American Earth Sciences*, *43*, 74–85. https://doi.org/10.1016/j.jsames.2012.12.009

Beucher, R., & Huismans, R. (2020). Morphotectonic evolution of passive margins undergoing active surface processes: Large-scale experiments using numerical models. *Geochemistry, Geophysics, Geosystems*, *21*, e2019GC008884. https://doi.org/10.1029/2019GC008884

Braun, J. (2018). A review of numerical modeling studies of passive margin escarpments leading to a new analytical expression for the rate of escarpment migration velocity. *Gondwana Research*, *53*, 209–224. https://doi.org/10.1016/j.gr.2017.04.012

Braun, J., & Beaumont, C. (1989). A physical explanation of the relation between flank uplifts and the breakup unconformity at rifted continental margins. *Geology*, *17*(8), 760–764. https://doi.org/10.1130/0091-7613(1989)017<0760:APEOTR>2.3.CO;2

Brune, S., Heine, C., Clift, P. D., & Pérez-Gussinyé, M. (2017). Rifted margin architecture and crustal rheology: Reviewing Iberia–Newfoundland, central South Atlantic, and South China Sea. *Marine and Petroleum Geology*, *79*, 257–281. https://doi.org/10.1016/j.marpetgeo.2016.10.018

Brune, S., Heine, C., Pérez-Gussinyé, M., & Sobolev, S. V. (2014). Rift migration explains continental margin asymmetry and crustal hyper-extension. *Nature Communications*, *5*(1), 1–9. https://doi.org/10.1038/ncomms5014

Burov, E. B., & Cloetingh, S. A. (1997). Erosion and rift dynamics: New thermomechanical aspects of post-rift evolution of extensional basins. *Earth and Planetary Science Letters*, *150*(1–2), 7–26. https://doi.org/10.1016/S0012-821X(97)00069-1

Burov, E. B., & Diament, M. (1995). The effective elastic thickness (T_e) of continental lithosphere: What does it really mean? *Journal of Geophysical Research*, *100*(B3), 3905–3927. https://doi.org/10.1029/94JB02770

Carminatti, M., Wolff, B., & Gamboa, L. (2008). *New exploratory frontiers in Brazil*. Paper presented at 19th World Petroleum Congress.

Cogné, N., Cobbold, P. R., Riccomini, C., & Gallagher, K. (2013). Tectonic setting of the Taubaté Basin (southeastern Brazil): Insights from regional seismic profiles and outcrop data. *Journal of South American Earth Sciences*, *42*, 194–204. https://doi.org/10.1016/j.jsames.2012.09.011

Cogné, N., Gallagher, K., & Cobbold, P. R. (2011). Post-rift reactivation of the onshore margin of southeast Brazil: Evidence from apatite (U–Th)/He and fission-track data. *Earth and Planetary Science Letters*, *309*(1–2), 118–130. https://doi.org/10.1016/j.epsl.2011.06.025

Cogné, N., Gallagher, K., Cobbold, P. R., Riccomini, C., & Gautheron, C. (2012). Post-breakup tectonics in southeast Brazil from thermochronological data and combined inverse-forward thermal history modeling. *Journal of Geophysical Research*, *117*, B11413. https://doi.org/10.1029/2012JB009340

Crameri, F., Schmeling, H., Golabek, G., Duretz, T., Orendt, R., Buiter, S., et al. (2012). A comparison of numerical surface topography calculations in geodynamic modelling: An evaluation of the 'sticky air' method. *Geophysical Journal International*, *189*(1), 38–54. https://doi.org/10.1111/j.1365-246X.2012.05388.x

Dunbar, J. A., & Sawyer, D. S. (1988). Continental rifting at pre-existing lithospheric weaknesses. *Nature*, *333*(6172), 450–452. https://doi.org/10.1038/333450a0

Gallagher, K., & Brown, R. (1999). Denudation and uplift at passive margins: The record on the Atlantic margin of southern Africa. *Philosophical Transactions of the Royal Society of London. Series A: Mathematical, Physical and Engineering Sciences*, *357*(1753), 835–859. https://doi.org/10.1098/rsta.1999.0354

Gerya, T. (2019). *Introduction to numerical geodynamic modelling*. Cambridge University Press.

Gilchrist, A., & Summerfield, M. (1990). Differential denudation and flexural isostasy in formation of rifted-margin upwarps. *Nature*, *346*(6286), 739–742. https://doi.org/10.1038/346739a0

Gilchrist, A. R., Kooi, H., & Beaumont, C. (1994). Post-Gondwana geomorphic evolution of southwestern Africa: Implications for the controls on landscape development from observations and numerical experiments. *Journal of Geophysical Research*, *99*(B6), 12211–12228. https://doi.org/10.1029/94JB00046

Gleason, G. C., & Tullis, J. (1995). A flow law for dislocation creep of quartz aggregates determined with the molten salt cell. *Tectonophysics*, *247*(1–4), 1–23. https://doi.org/10.1016/0040-1951(95)00011-b

Heténi, M. (1946). *Beams on elastic foundation: Theory with applications in the fields of civil and mechanical engineering*. University of Michigan Press.

Hiruma, S. T., Riccomini, C., Modenesi-Gauttieri, M. C., Hackspacher, P. C., Neto, J. C. H., & Franco-Magalhães, A. O. (2010). Denudation history of the Bocaina Plateau, Serra do Mar, southeastern Brazil: Relationships to Gondwana breakup and passive margin development. *Gondwana Research*, *18*(4), 674–687. https://doi.org/10.1016/j.gr.2010.03.001

Huismans, R. S., & Beaumont, C. (2003). Symmetric and asymmetric lithospheric extension: Relative effects of frictional-plastic and viscous strain softening. *Journal of Geophysical Research*, *108*(B10), 2496. https://doi.org/10.1029/2002JB002026

Huismans, R. S., & Beaumont, C. (2014). Rifted continental margins: The case for depth-dependent extension. *Earth and Planetary Science Letters*, *407*, 148–162. https://doi.org/10.1016/j.epsl.2014.09.032

Karato, S., & Wu, P. (1993). Rheology of the upper mantle: A synthesis. *Science*, *260*(5109), 771–778. https://doi.org/10.1126/science.260.5109.771

Karner, G. D. (2000). Rifts of the Campos and Santos basins, southeastern Brazil: Distribution and timing. In M. Mello & B. Katz (Eds.), *Petroleum systems of South Atlantic margins* (Vol. 73, pp. 301–315). https://doi.org/10.1306/M73705C21

Karner, G. D., & Gambôa, L. A. P. (2007). Timing and origin of the South Atlantic pre-salt sag basins and their capping evaporites. *Geological Society, London, Special Publications*, *285*(1), 15–35. https://doi.org/10.1144/SP285.2

Kooi, H., & Beaumont, C. (1994). Escarpment evolution on high-elevation rifted margins: Insights derived from a surface processes model that combines diffusion, advection, and reaction. *Journal of Geophysical Research*, *99*(B6), 12191–12209. https://doi.org/10.1029/94JB00047

Lavier, L. L., & Manatschal, G. (2006). A mechanism to thin the continental lithosphere at magma-poor margins. *Nature*, *440*(7082), 324–328. https://doi.org/10.1038/nature04608

Lavier, L. L., & Steckler, M. S. (1997). The effect of sedimentary cover on the flexural strength of continental lithosphere. *Nature*, *389*(6650), 476–479. https://doi.org/10.1038/39004

Meisling, K. E., Cobbold, P. R., & Mount, V. S. (2001). Segmentation of an obliquely rifted margin, Campos and Santos basins, southeastern Brazil. *AAPG Bulletin*, *85*(11), 1903–1924. https://doi.org/10.1306/8626D0A9-173B-11D7-8645000102C1865D

Moreira, J. L. P., Madeira, C. V., Gil, J. A., & Machado, M. A. P. (2007). Bacia de Santos. *Boletim de Geociencias da Petrobras*, *15*(2), 531–549.

Moresi, L., & Solomatov, V. (1998). Mantle convection with a brittle lithosphere: Thoughts on the global tectonic styles of the Earth and Venus. *Geophysical Journal International*, *133*(3), 669–682. https://doi.org/10.1046/j.1365-246X.1998.00521.x

Pérez-Gussinyé, M., Andrés-Martínez, M., Araújo, M., Xin, Y., Armitage, J., & Morgan, J. (2020). Lithospheric strength and rift migration controls on synrift stratigraphy and breakup unconformities at rifted margins: Examples from numerical models, the Atlantic and South China Sea margins. *Tectonics*, *39*, e2020TC006255. https://doi.org/10.1029/2020TC006255

Riccomini, C. (1989). *O rift continental do sudeste do Brasil* (Unpublished doctoral dissertation). Universidade de São Paulo. https://doi.org/10.11606/T.44.1990.tde-18032013-105507

Riccomini, C., Sant'Anna, L. G., & Ferrari, A. L. (2004). Evolução geológica do rift continental do sudeste do Brasil. *Geologia do continente Sul-Americano: evolução da obra de Fernando Flávio Marques de Almeida* (pp. 383–405).

Rigoti, C. A. (2015). *Evolução tectônica da Bacia de Santos com ênfase na geometria crustal: Interpretação integrada de dados de sísmica de reflexão e refração, gravimetria e magnetometria* (Unpublished doctoral dissertation). Dissertação de mestrado. Universidade Federal do Rio de Janeiro. http://www.bdtd.uerj.br/handle/1/7131

Sacek, V. (2017). Post-rift influence of small-scale convection on the landscape evolution at divergent continental margins. *Earth and Planetary Science Letters*, *459*, 48–57. https://doi.org/10.1016/j.epsl.2016.11.026

Sacek, V., Braun, J., & Van Der Beek, P. (2012). The influence of rifting on escarpment migration on high elevation passive continental margins. *Journal of Geophysical Research*, *117*, B04407. https://doi.org/10.1029/2011JB008547

Salazar-Mora, C. A., Huismans, R. S., Fossen, H., & Egydio-Silva, M. (2018). The Wilson cycle and effects of tectonic structural inheritance on rifted passive margin formation. *Tectonics*, *37*, 3085–3101. https://doi.org/10.1029/2018TC004962

Salgado, A. A., Marent, B. R., Cherem, L. F., Bourlès, D., Santos, L. J., Braucher, R., et al. (2014). Denudation and retreat of the Serra do Mar escarpment in Southern Brazil derived from in situ-produced ^{10}Be concentration in river sediment. *Earth Surface Processes and Landforms*, *39*(3), 311–319. https://doi.org/10.1002/esp.3448

Salomon, E., Koehn, D., & Passchier, C. (2015). Brittle reactivation of ductile shear zones in NW Namibia in relation to South Atlantic rifting. *Tectonics*, *34*, 70–85. https://doi.org/10.1002/2014TC003728

Silva, R. M., & Sacek, V. (2019). Shallow necking depth and differential denudation linked to post-rift continental reactivation: The origin of the Cenozoic basins in southeastern Brazil. *Terra Nova*, *31*(6), 527–533. https://doi.org/10.1111/ter.12423

Sternai, P. (2020). Surface processes forcing on extensional rock melting. *Scientific Reports*, *10*(1), 1–13. https://doi.org/10.1038/s41598-020-63920-w

Tetreault, J., & Buiter, S. (2018). The influence of extension rate and crustal rheology on the evolution of passive margins from rifting to break-up. *Tectonophysics*, *746*, 155–172. https://doi.org/10.1016/j.tecto.2017.08.029

Theunissen, T., & Huismans, R. S. (2019). Long-term coupling and feedback between tectonics and surface processes during non-volcanic rifted margin formation. *Journal of Geophysical Research: Solid Earth*, *124*, 12323–12347. https://doi.org/10.1029/2018JB017235

Tommasi, A., & Vauchez, A. (2001). Continental rifting parallel to ancient collisional belts: An effect of the mechanical anisotropy of the lithospheric mantle. *Earth and Planetary Science Letters*, *185*(1–2), 199–210. https://doi.org/10.1016/S0012-821X(00)00350-2

Tommasi, A., & Vauchez, A. (2015). Heterogeneity and anisotropy in the lithospheric mantle. *Tectonophysics*, *661*, 11–37. https://doi.org/10.1016/j.tecto.2015.07.026

Trouw, R. A. J., Heilbron, M., Ribeiro, A., Paciullo, F., Valeriano, C., Almeida, J., & Andreis, R. (2000). The central segment of the Ribeira Belt. *Tectonic Evolution of South America*, *31*, 287–310.

Turcotte, D. L., & Schubert, G. (2002). *Geodynamics*. Cambridge University Press.

van der Beek, P., Summerfield, M. A., Braun, J., Brown, R. W., & Fleming, A. (2002). Modeling postbreakup landscape development and denudational history across the southeast African (Drakensberg Escarpment) margin. *Journal of Geophysical Research*, *107*(B12), ETG 11-1–ETG 11–18. https://doi.org/10.1029/2001JB000744

Zalán, P. V., Severino, M. D. C. G., Rigoti, C. A., Magnavita, L. P., Oliveira, J. A. B., & Vianna, A. R. (2011). An entirely new 3D-view of the crustal and mantle structure of a South Atlantic passive margin—Santos, Campos and Espírito Santo Basins, Brazil. *AAPG Search and Discovery Article #30177, AAPG Annual Convention 2011, Houston, Texas, April 10–13* (p. 12). (Expanded Abstract).